Computational Materials Science 212 (2022) 111556

Contents lists available at ScienceDirect

Computational Materials Science

journal homepage: www.elsevier.com/locate/commatsci

Full Length Article

Application of scalar auxiliary variable scheme to phase-field equations

Rui Wang [a], Yanzhou Ji [a], Jie Shen [b,*], Long-Qing Chen [a,*]

[a] Department of Materials Science and Engineering, The Pennsylvania State University, University Park, PA 16802, United States
[b] Department of Mathematics, Purdue University, West Lafayette, IN 47907, United States

ARTICLE INFO

Keywords:
Scalar auxiliary variable (SAV) scheme
Phase-field method
Grain growth
Phase separation
Precipitation

ABSTRACT

It has been a continuing challenge to carry out simulations at time and spatial scales compatible with practical experimental observations. Here we implement a novel scalar auxiliary variable (SAV) scheme introduced in (Shen et al., 2018) for phase-field equations to drastically improve the numerical accuracy, efficiency and stability. We first bench-marked two representative phase-field method applications involving three-dimensional (3D) grain growth and spinodal phase separation. By implementing the SAV scheme within the state-of-the-art semi-implicit Fourier spectral scheme we achieved an order of magnitude improvement for the single-order-parameter Allen-Cahn equation and at least a 100% improvement for a set of multi-order-parameter Allen-Cahn equations for grain growth problems and the Cahn-Hilliard equation for compositional phase separation. More importantly, the efficiency enhancement of SAV becomes more dramatic as interfaces become sharper. Its application to the growth morphology and kinetics of β'-Mg_7Nd precipitates demonstrates a remarkable improvement of more than 50 times in computational time. This work is expected to further stimulate the applications of phase-field simulations of a broad range of materials processes.

1. Introduction

Phase-field method is a versatile and yet computationally expensive method that has been applied to modeling, understanding, and predicting microstructure evolution in a wide variety of material processes [1]. There are continuing demands for large-scale three-dimensional (3D) simulations [2,3] with realistic time scales and spatial resolutions that are compatible with experimental observations. Many attempts have been made to develop and implement advanced algorithms to improve the efficiency and accuracy of the numerical solutions for phase-field evolution equations [4-21]. A number of progresses have been made in demonstrating significant efficiency improvement with good applicability across different phase-field models [4,6] as well as in optimizing existing algorithms and numerical treatments [18,19,22]. Among these efforts, the application of the semi-implicit Fourier spectral method to phase-field equations by Chen *et al.* [6] plays an important role, bringing in 2–3 orders of magnitude efficiency upgrade after solving the elliptical terms semi-implicitly with the help of Fourier spectral method. This greatly helps the algorithm development in different aspects of phase-field applications such as coupled Cahn-Hillard/Navier-Stokes system by Badalassi *et al.* [4], polycrystal growth under multiple coupled Allen-Cahn equations [23,24] and ferroelectric domain evolution coupling with elastics [25].

Recently, an unconditionally energy stable and efficient numerical scheme called Invariant Energy Quadratization (IEQ) scheme has been developed by Yang *et al.* [21] which is successfully implemented to solve phase-field equations. The seminal idea of this work was to evolve the gradient energy term and other energy terms separately while keeping the kinetics and energy dissipation law very similar, so the non-linear system can be simplified to coupling linear system which can be efficiently solved. However, the IEQ scheme has drawbacks such as variable coefficients while solving the linear equations and the requirement that energy density should be bounded below. Shen *et al.* [14] then proposed a novel Scalar Auxiliary Variable (SAV) scheme which inherits the advantages in IEQ scheme such as the separation of evolving different energy terms, good accuracy and unconditionally energy stability, where the energy of the system always decreases regardless of time stepping. See ref. [14] and the supplemental material for the proof. Moreover, in the SAV scheme, a variable has been introduced to help evolve the non-gradient free energy term while linear equations with constant coefficients are solved. Also, the requirement of non-linear energy density being bounded from below has been alleviated. For the SAV scheme, stability analyses are performed in [14,26] and asymptotic behavior is discussed in [27,28] which proves the scheme is accurate in

* Corresponding authors.
E-mail addresses: shen7@purdue.edu (J. Shen), lqc3@psu.edu (L.-Q. Chen).

https://doi.org/10.1016/j.commatsci.2022.111556
Received 8 May 2022; Accepted 23 May 2022
Available online 18 June 2022

Allen-Cahn and Cahn-Hillard equations in backward differentiation formula (BDF). This newly-proposed scheme provides a way for accelerating phase-field simulations with good applicability.

In this paper, we implement the Scalar Auxiliary Variable (SAV) scheme [14,29] to solve the phase-field evolution equations. With the discretized evolution equations firstly derived in this work for Allen-Cahn and Cahn-Hillard equations-based phase-field models, we will demonstrate that the SAV scheme is not only easy to implement but also numerically accurate, efficient and unconditionally stable in solving phase-field equations. We first investigated its performance using two typical application examples. One is the three-dimensional (3D) grain growth kinetics by solving a large set of coupled Allen-Cahn equations, and the other is spinodal phase separation described by Cahn-Hilliard equations. We then applied it to model the growth morphology and kinetics of precipitates in a Mg-alloy.

In the following, we present the SAV scheme in Section 2. Section 3 describes the implementation of the SAV scheme in solving phase-field equations for 3D grain growth and 3D phase separation in combination with the semi-implicit Fourier-spectral scheme. Section 3 focuses on benchmark testing results on 3D grain growth and phase separation and discuss the efficiency, accuracy, and stability of the SAV scheme by comparing with existing state-of-the-art semi-implicit Fourier spectral scheme. Section 3 discusses the application of the SAV scheme to the growth morphology and kinetics of a Mg-alloy incorporating coherency strain energy contribution. The last section discusses the details about implementing the SAV scheme and potential strategies to further improve the efficiency.

2. SAV scheme and numerical implementation

We consider a system described by a set of spatially dependent field variables with its total free energy F given by

$$F = \int_V \left[f(\{\eta_i\}) + \sum\nolimits_{p,q}^{N} \frac{\kappa_{pq}}{2} \nabla\eta_p \nabla\eta_q \right] \mathrm{d}V, \tag{1}$$

where f is the local free energy density as a function of N field variables $\eta_1, \eta_2, \cdots, \eta_N$, and $\boldsymbol{\kappa}$ is the gradient coefficient matrix with components κ_{pq}.

The evolution of field variables $\boldsymbol{\eta} = (\eta_1, \eta_2, \cdots, \eta_N)^T$ follows

$$\frac{\partial \boldsymbol{\eta}}{\partial t} = \mathscr{G}\boldsymbol{\mu}, \tag{2}$$

where $\mathscr{G} = -(-\Delta)^x \mathbf{L}, (x = 0, 1)$ is a non-positive symmetric operator corresponding to the Allen-Cahn ($x = 0$) or the Cahn-Hilliard ($x = 1$) equation with $\mathbf{L}$ being the kinetic coefficient matrix, $\boldsymbol{\mu}$ represents the driving force for the evolution of field variables $\boldsymbol{\eta}$ and is defined as

$$\boldsymbol{\mu} \equiv \frac{\delta F}{\delta \boldsymbol{\eta}} = -\mathbf{D}\boldsymbol{\kappa}\Delta\boldsymbol{\eta} + \mathbf{f}'(\{\eta_i\}), \tag{3}$$

where $\mathbf{D} = \frac{1}{2}\boldsymbol{J}_{N,N} + \frac{1}{2}\boldsymbol{I}_N$ is the coefficient matrix with $\boldsymbol{J}$ and $\boldsymbol{I}$ being the matrix of ones and the identity matrix, respectively, and $\mathbf{f}'(\{\eta_i\}) = (\partial f(\{\eta_i\})/\partial\eta_1, \partial f(\{\eta_i\})/\partial\eta_2, \cdots, \partial f(\{\eta_i\})/\partial\eta_N)^T$.

To solve the evolution equation (Eq. (2)), the SAV scheme introduces a temporally evolving scalar auxiliary variable, r, with its initial value defined as

$$r|_{t=0} = \sqrt{\mathscr{F}_L|_{t=0} + C_0} \tag{4}$$

where $\mathscr{F}_L = \int_V f(\{\eta_i\})\mathrm{d}V$ is the total local free energy which evolves according to the order parameter set $\{\eta_i\}$ and is bounded below regardless of simulation time, i.e., a value of C_0 such that $C_0 \geq -\mathscr{F}_L$ to ensure that the quantity inside the square root of Eq. (4) is always positive. Following the SAV scheme [14], Eq. (3) is now rewritten as

$$\boldsymbol{\mu} = -\mathbf{D}\boldsymbol{\kappa}\Delta\boldsymbol{\eta} + \frac{r}{\sqrt{\mathscr{F}_L + C_0}}\mathbf{f}'(\{\eta_i\}). \tag{5}$$

It should be noted that the scalar auxiliary variable r temporally evolves independently in a sense that $r(t > 0) \approx \sqrt{\mathscr{F}_L + C_0}$, and the evolution of r is described [14] by

$$\frac{\mathrm{d}r}{\mathrm{d}t} = \frac{1}{2\sqrt{\mathscr{F}_L + C_0}} \int_V \sum\nolimits_q^N f_q'(\{\eta_i\}) \frac{\partial \eta_q}{\partial t} \mathrm{d}V \tag{6}$$

where $f_q'(\{\eta_i\}) \equiv \partial f(\{\eta_i\})/\partial\eta_q$. According to [14], the SAV scheme as described in Eqs. (1), (2), (5), (6) is unconditionally energy-stable and accurate based on appropriate discretization. It should be noted that the SAV scheme is a numerical method which does not change the dynamics of the evolution equation [14,26-28]. Since Eq. (6) is a full derivative of the equation $r = \sqrt{\mathscr{F}_L + C_0}$, this means the coefficient $\frac{r}{\sqrt{\mathscr{F}_L + C_0}}$ reaches unity when time stepping is sufficiently small.

In order to numerically evolve Eqs. (2), (5), and (6), we discretize the system using the 1st order backward differentiation formula (BDF) with equal time stepping Δt within the semi-implicit scheme,

$$\frac{\boldsymbol{\eta}^{n+1} - \boldsymbol{\eta}^n}{\Delta t} = \mathscr{G}\boldsymbol{\mu}^{n+1}, \tag{7}$$

$$\boldsymbol{\mu}^{n+1} = -\boldsymbol{\kappa}\Delta\boldsymbol{\eta}^{n+1} + \frac{r^{n+1}}{\overline{r^{n+1}}}\mathbf{f}'\left(\{\overline{\eta_i^{n+1}}\}\right), \tag{8}$$

$$r^{n+1} - r^n = \frac{1}{2\overline{r^{n+1}}} \int_V \sum\nolimits_q^N f_q'\left(\{\overline{\eta_i^{n+1}}\}\right)\left(\eta_q^{n+1} - \eta_q^n\right)\mathrm{d}V, \tag{9}$$

where the superscripts n and $n+1$ correspond to variables at the n^{th} and the $n+1^{\text{th}}$ time steps, respectively. In this work, we assume no cross-interaction between order parameters, i.e. $\kappa_{pq} = 0 (p \neq q)$, so $\mathbf{D}\boldsymbol{\kappa} = \boldsymbol{\kappa}$ after the assumption. In order to obtain the variables of the $n+1^{\text{th}}$ step based on the values of previous steps in semi-implicit scheme, an explicit approximation of the field variable matrix at the $n+1^{\text{th}}$ step, $\overline{\boldsymbol{\eta}^{n+1}}$, is needed, and we use

$$\overline{\boldsymbol{\eta}^{n+1}} = 2\boldsymbol{\eta}^n - \boldsymbol{\eta}^{n-1} \tag{10}$$

The approximated scalar auxiliary variable $\overline{r^{n+1}}$ can be expressed based on Eq. (4) using the approximated field variable $\overline{\boldsymbol{\eta}^{n+1}}$:

$$\overline{r^{n+1}} = \sqrt{\int_V f(\{\overline{\eta_i^{n+1}}\})\mathrm{d}V + C_0}. \tag{11}$$

Combining Eqs. (7)- (9)and eliminating $\boldsymbol{\mu}^{n+1}$ and r^{n+1}, we find

$$\boldsymbol{\eta}^{n+1} - \boldsymbol{\eta}^n = \Delta t \cdot \mathscr{G}\left\{ -\boldsymbol{\kappa}\Delta\boldsymbol{\eta}^{n+1} + \overline{\mathbf{b}^{n+1}}\left[r^n + \int_V \sum\nolimits_q^N \frac{\overline{b_q^{n+1}}}{2}\left(\eta_q^{n+1} - \eta_q^n\right)\mathrm{d}V \right] \right\}, \tag{12}$$

where $\overline{\mathbf{b}^{n+1}} = \left(\overline{b_1^{n+1}}, \overline{b_2^{n+1}}, \cdots, \overline{b_N^{n+1}}\right)^T = \mathbf{f}'\left(\{\overline{\eta_i^{n+1}}\}\right)/\overline{r^{n+1}}$. By separating the unknown variables and the known ones, the expression can be rearranged as

$$\begin{aligned} &\boldsymbol{\eta}^{n+1} + \Delta t \cdot \mathscr{G}\boldsymbol{\kappa}\Delta\boldsymbol{\eta}^{n+1} - \frac{\Delta t}{2}\sum\nolimits_q^N \left(\overline{b_q^{n+1}}, \eta_q^{n+1}\right)\mathscr{G}\overline{\mathbf{b}^{n+1}} \\ &= \boldsymbol{\eta}^n + \Delta t\left[r^n - \frac{1}{2}\sum\nolimits_q^N \left(\overline{b_q^{n+1}}, \eta_q^n\right) \right]\mathscr{G}\overline{\mathbf{b}^{n+1}}, \end{aligned} \tag{13}$$

where $\left(\overline{b_q^{n+1}}, \eta_q^n\right) = \int_V \overline{b_q^{n+1}}(V)\eta_q^n(V)\,\mathrm{d}V$ represents the inner product of the two scalar fields $\overline{b_q^{n+1}}$ and η_q^n. We further define $\left(\overline{\mathbf{b}^{n+1}}, \boldsymbol{\eta}^n\right) = \left(\left(\overline{b_1^{n+1}}, \eta_1^n\right), \left(\overline{b_2^{n+1}}, \eta_2^n\right), \cdots, \left(\overline{b_N^{n+1}}, \eta_N^n\right)\right)^T$ as the inner product matrix,

$\mathbf{C}^n = \boldsymbol{\eta}^n + \Delta t\left[r^n - \frac{1}{2}\sum_q^N\left(\overline{b_q^{n+1}}, \eta_q^n\right)\right]\mathscr{G}\overline{\mathbf{b}^{n+1}}$ as the constant matrix in Eq. (13), and $\mathbf{M} = \boldsymbol{I}_N + \Delta t\cdot\mathscr{G}\boldsymbol{\kappa}\Delta$ as the coefficient matrix for $\boldsymbol{\eta}^{n+1}$, so that the field variables at the $n+1^{\text{th}}$ step can be obtained by solving

$$\mathbf{M}\boldsymbol{\eta}^{n+1} - \frac{\Delta t}{2}\boldsymbol{J}_{1,N}\left(\overline{\mathbf{b}^{n+1}}, \eta^{n+1}\right)\mathscr{G}\overline{\mathbf{b}^{n+1}} = \mathbf{C}^n. \tag{14}$$

Premultiply Eq. (14) with $\mathbf{M}^{-1}$, take inner product of both sides with respect to $\overline{\mathbf{b}^{n+1}}$, and then premultiply both sides with $\boldsymbol{J}_{1,N}$, one could get

$$\begin{aligned}\boldsymbol{J}_{1,N}\left(\overline{\mathbf{b}^{n+1}}, \boldsymbol{\eta}^{n+1}\right) - \frac{\Delta t}{2}\boldsymbol{J}_{1,N}\left(\overline{\mathbf{b}^{n+1}}, \boldsymbol{\eta}^{n+1}\right)\boldsymbol{J}_{1,N}\left(\overline{\mathbf{b}^{n+1}}, \mathbf{M}^{-1}\mathscr{G}\overline{\mathbf{b}^{n+1}}\right)\\ = \boldsymbol{J}_{1,N}\left(\overline{\mathbf{b}^{n+1}}, \mathbf{M}^{-1}\mathbf{C}^n\right).\end{aligned} \tag{15}$$

Now the unknown inner product term $\boldsymbol{J}_{1,N}\left(\overline{\mathbf{b}^{n+1}}, \boldsymbol{\eta}^{n+1}\right)$ in Eqs. (9) and (14) can be explicitly expressed as

$$\boldsymbol{J}_{1,N}\left(\overline{\mathbf{b}^{n+1}}, \boldsymbol{\eta}^{n+1}\right) = \frac{\boldsymbol{J}_{1,N}\left(\overline{\mathbf{b}^{n+1}}, \mathbf{M}^{-1}\mathbf{C}^n\right)}{1 - \frac{\Delta t}{2}\boldsymbol{J}_{1,N}\left(\overline{\mathbf{b}^{n+1}}, \mathbf{M}^{-1}\mathscr{G}\overline{\mathbf{b}^{n+1}}\right)}. \tag{16}$$

Combining Eqs. (9), (14), and (16) the variables at the $n+1^{\text{th}}$ step can be obtained,

$$\boldsymbol{\eta}^{n+1} = \mathbf{M}^{-1}\mathbf{C}^n + \frac{\Delta t}{2}\frac{\boldsymbol{J}_{1,N}\left(\overline{\mathbf{b}^{n+1}}, \mathbf{M}^{-1}\mathbf{C}^n\right)}{1 - \frac{\Delta t}{2}\boldsymbol{J}_{1,N}\left(\overline{\mathbf{b}^{n+1}}, \mathbf{M}^{-1}\mathscr{G}\overline{\mathbf{b}^{n+1}}\right)}\mathbf{M}^{-1}\mathscr{G}\overline{\mathbf{b}^{n+1}}, \tag{17}$$

$$r^{n+1} = r^n + \frac{\boldsymbol{J}_{1,N}\left(\overline{\mathbf{b}^{n+1}}, \mathbf{M}^{-1}\mathbf{C}^n\right)}{2 - \Delta t\cdot\boldsymbol{J}_{1,N}\left(\overline{\mathbf{b}^{n+1}}, \mathbf{M}^{-1}\mathscr{G}\overline{\mathbf{b}^{n+1}}\right)} - \frac{1}{2}\boldsymbol{J}_{1,N}\left(\overline{\mathbf{b}^{n+1}}, \eta^n\right). \tag{18}$$

It should be noted that the premultiplication of $\boldsymbol{J}_{1,N} = (1, 1, \cdots, 1)$ is equivalent to taking summation of the original $N\times 1$ matrix for all of its components, and the operator $\mathbf{M}$ is diagonal since the gradient coefficient matrix $\boldsymbol{\kappa}$ is diagonal. As a result, Eqs. (17) and (18) can be easily and efficiently solved. In addition, Eqs. (17) and (18) are general and independent of the numerical schemes (e.g., finite difference, finite element, Fourier spectral method, etc.) and specific free energy expressions. In the examples presented blow, the Fourier spectral scheme is used. (See supplementary material S5 for the detailed strategy of solving Eqs. (17) and (18) utilizing Fourier transform).

It should be pointed out that a 2^{nd} order BDF based SAV scheme can be discretized similarly, and the Crank-Nicolson (CN) scheme is also applicable in the SAV approach with an even simpler implementation (see supplementary material Section S1 and S2 for detailed implementation of 2^{nd} order BDF based and CN based SAV schemes).

3. Applications of SAV scheme

3.1. Shrinking of a 3D single antiphase domain

We benchmark the efficiency of the SAV scheme using the shrinking rate of a 3D spherical antiphase domain as an example. A simplest form of $f(\eta)$ to describe the shrinking of a single antiphase domain is the double-well energy density function [23,24]:

$$f(\eta) = -\frac{1}{2}\eta^2 + \frac{1}{4}\eta^4, \tag{19}$$

where $f(\eta)$ has two degenerated minima located at $\eta = -1, +1$, representing two antiphase domain states. For this example, the governing evolution equation is

$$\frac{\partial\eta}{\partial t} = L\kappa\Delta\eta - Lf'(\eta), \tag{20}$$

where

$$f'(\eta) = -\eta + \eta^3. \tag{21}$$

Following Eqs. (7)-(9), the discretized evolution equations based on the SAV scheme with 1^{st} order BDF are given by

$$\frac{\eta^{n+1} - \eta^n}{\Delta t} = -L\left(-\kappa\Delta\eta^{n+1} + \frac{r^{n+1}}{\overline{r^{n+1}}}f'\left(\overline{\eta^{n+1}}\right)\right), \tag{22}$$

$$r^{n+1} - r^n = \frac{1}{2\overline{r^{n+1}}}\int_V f'\left(\overline{\eta^{n+1}}\right)\left(\eta^{n+1} - \eta^n\right)\mathrm{d}V. \tag{23}$$

η^{n+1} and r^{n+1} can then be obtained following Eqs. (17) and (18) using $M = 1 - \Delta t\cdot L\kappa\Delta$, $C^n = \eta^n - \Delta t\left[r^n - \frac{1}{2}\left(\overline{b^{n+1}}, \eta^n\right)\right]L\overline{b^{n+1}}$, $\overline{b^{n+1}} = f'\left(\overline{\eta^{n+1}}\right)/\overline{r^{n+1}}$ and $\overline{r^{n+1}} = \sqrt{\int_V f(\overline{\eta^{n+1}})\mathrm{d}V + C_0}$ with $\overline{\eta^{n+1}} = 2\eta^n - \eta^{n-1}$ and $C_0 = V/4$ where V is the volume of the system.

The simulation starts with one spherical antiphase domain with radius R_0 in a 3D periodic system. As illustrated in Fig. 1 (a), the initial profile of η is defined as $\eta(\ell - \ell_0 \leqslant R_0)|_{t=0} = 1$ and $\eta(\ell - \ell_0 > R_0)|_{t=0} = -1$, where ℓ is the position vector for any points, and ℓ_0 is the position vector for the center of the spherical domain. The simulation parameters and their descriptions are listed in Table 1. The Lx, Ly and Lz are the dimensions for the simulation region and Δx, Δy and Δz are the dimensions for one mesh along, y and z directions, respectively. nx, ny and nz are numbers of mesh points along the corresponding directions, e.g., nx = Lx/Δx. In this work, both cubic meshes ($\Delta x = \Delta y = \Delta z$) and cubic simulation region (Lx = Ly = Lz) are used. During the evolution, the radius of the spherical antiphase domain will decrease with time, as shown in Fig. 1(b) to minimize the total interfacial energy. When the driving force or kinetic coefficient is small, i.e., L and κ are small, the radius $R(t)$ of the shrinking domain can be expressed analytically as $R(t) = \sqrt{R_0^2 - 4L\kappa t}$, which is used for quantifying the accuracy. As shown in Fig. 1 (c), the simulated decreasing trend of $R(t)$, under $\Delta x = 0.33$ and $\Delta t = 0.5$, agrees well with the reference solution. To further quantify the simulation accuracy, we define $\mathscr{R} := \left(R_0^2 - R^2(t)\right)/4L\kappa t$ and compare it with the reference value of 1.0 in Fig. 1 (d) as a function of time. The parameter $|1 - \mathscr{R}|$ is then used to quantify the error for the current problem, which is <0.2% for the simulation example in Fig. 1.

We then systematically investigate the accuracy of the 1^{st} and 2^{nd} order BDF based SAV schemes (*abbr.* 1stSAV and 2ndSAV, respectively) under different discretization grid sizes (Δx) and time step sizes (Δt) for the current problem, and compare the simulation results with the generally accepted discretization schemes in phase-field models, such as explicit differentiation scheme [23,24] (in short, Explicit) and both 1^{st} and 2^{nd} BDF based semi-implicit (SI) schemes [6] (*abbr.* 1stSI and 2ndSI respectively). (See supplemental material Section S3 for full descriptions and equations for the numerical schemes that are not elaborated in the main paper.) The Explicit scheme is implemented using the finite difference method whereas the other schemes use the Fourier spectral method to avoid solving matrices [6].

A series of simulations are performed using the SAV-based scheme with comparison of well-accepted discretization of phase-field models. In Fig. 2, different time stepping Δts are used on the antiphase shrinking problem to examine the accuracy of the models. As shown in Fig. 2 (a), under $\kappa = 1$, the error $|1 - \mathscr{R}|$ increases with the increase of Δt, and decreases with the increase of nx, until reaching a stable error value or the numerical scheme diverges (e.g., $\Delta t = 0.01$, nx greater than 260 for the explicit scheme). In addition, the critical value for nx for the error to reach a stable magnitude decreases with the increase of Δt. These observations are consistent with the prediction from the truncation errors of the numerical schemes. More importantly, the accuracy and applicability range of the numerical schemes are different: the 1stSI is accurate ($|1 - \mathscr{R}| < 5\%$) only when $\Delta t = 0.01$ and n$x \geq 100$; the accuracies of the 2ndSI, 1stSAV and 2ndSAV schemes are comparable when n$x \geq 100$ ($\Delta x \leq 1$) for all three Δt values, while 2ndSAV is not as accurate as

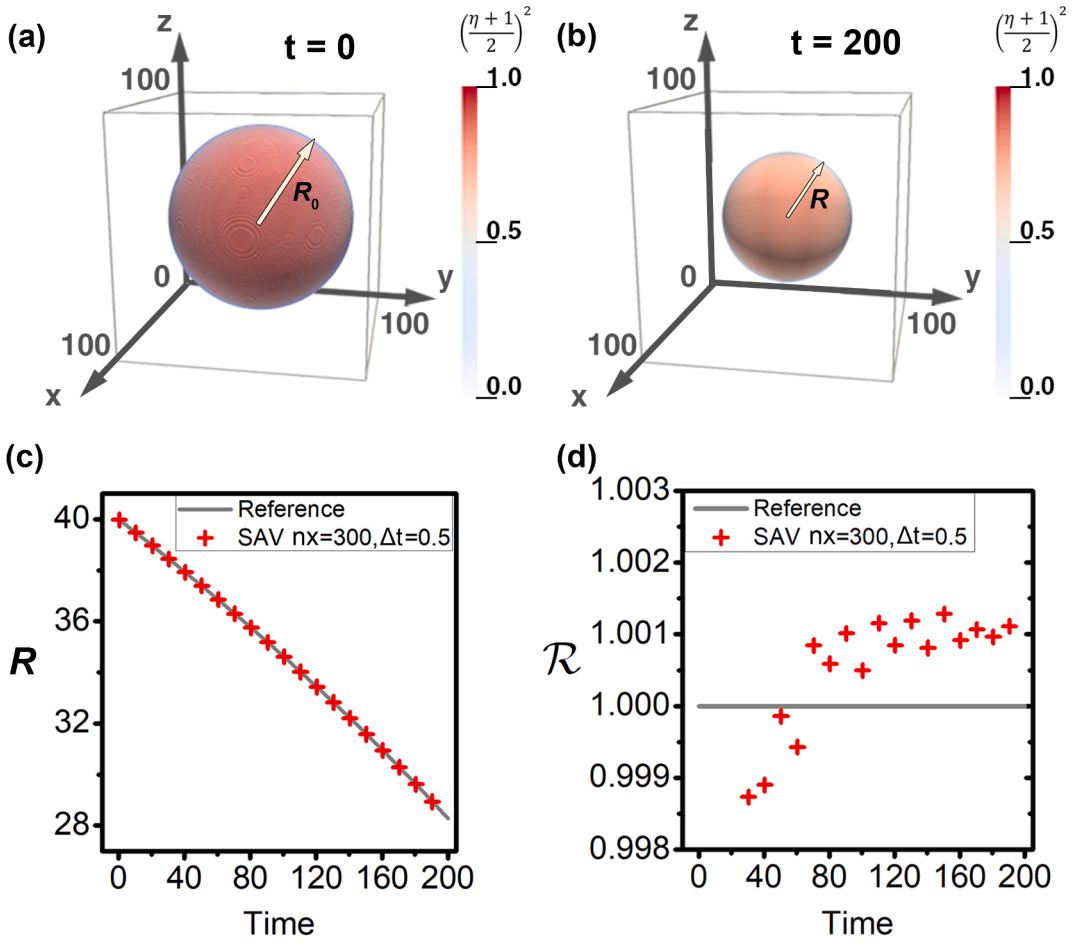

Fig. 1. Simulation setup and demonstration for 3D single spherical grain shrinking problem and its accuracy quantification. (a) (b) the 3D view for the single spherical grain at $t = 0$ and $t = 200$, respectively. In these plots, the region that $\eta < 0$ are set to be transparent to show the spherical grain. (c) (d) the grain radius R vs. t plot and $\mathscr{R} := \left(R_0^2 - R^2(t)\right)/4L\kappa t$ vs. t plot for the SAV incorporated model with $nx = ny = nz = 300$, $\Delta t = 0.5$, respectively, where $nx = Lx/\Delta x$. (d) provides a clearer error estimation compared with (c). All simulations shown in this figure adopt parameters in Table 1.

Table 1
Parameters used in the 3D single spherical grain shrinking simulation. κ and L are the parameters introduced in Eqs. (2), (3) and (20), while κ and L are reduced to scalars from matrices since only one order parameter is used, i.e. $N = 1$. Lx, Ly and Lz are the dimensions of the simulation system along x,y and z direction, respectively, while Δx, Δy and Δz are the dimensions of the discretized mesh.

κ	L	N	$Lx(=Ly=Lz)$	$\Delta x(=\Delta y=\Delta z)$	Δt	R_0
0.01–1	1	1	100	0.5	0.01–20	40

the other two schemes when $nx \leq 100$ ($\Delta x \geq 1$). Thus, in terms of the current domain shrinking problem, the accuracy and applicability of 1stSAV scheme is better than 2ndSAV for most of the testing ranges of $0.33 \leq \Delta x \leq 2$ and $0.01 \leq \Delta t \leq 7.7$; moreover, under a fixed Δx, its adoptable Δt value is over an order of magnitude larger than the best reference schemes (explicit and SI schemes) at a comparable accuracy. The 2ndSAV scheme is the most accurate when both Δx and Δt are small.

Another potential advantage of the SAV scheme is its capability to dealing with microstructure evolution problems with a very thin interfacial thickness. We performed a series of simulations under a fixed mesh size $\Delta x = 0.5$ while varying Δt and the gradient coefficient values, $\kappa = 1, 0.1$ and 0.01, which is positively correlated to the equilibrium interfacial thickness based on the form of Eq. (1). In this work, the interfacial thickness is defined as the area with $\eta \in [0.1, 0.9]$. For the simulation results shown in Fig. 2 (b)-(d), we determine whether a result is accurate based on the following two criteria: (1) The error for the radius of the shrinking domain should be <5%, i.e., $|1 - \mathscr{R}| < 5\%$; (2) the maximum value of the order parameter inside the shrinking domain, η_{max}, deviates no more than 5% from its equilibrium value ($\eta = 1$), i.e., $|\eta_{max} - 1| < 5\%$. In Fig. 2 (b)-(d), a cross mark is labeled when a simulation result does not meet either of the two criteria. According to Fig. 2 (b), for the $\kappa = 1$ case, the explicit scheme diverges when $\Delta t \geq 0.04$. For SI schemes, even though they are stable for larger Δt, the accuracy drops as Δt increases: the 1stSI scheme results in an inaccurate radius for $\Delta t \geq 0.1$, while the error in the order parameter values for 2ndSI scheme fails to satisfy the criterion $|\eta_{max} - 1| < 5\%$ for $\Delta t \geq 0.6$. On the other hand, for the SAV schemes, the Δt ranges which yield sufficient solution accuracies are significantly expanded: the maximum accurate Δt for 1stSAV ($\Delta t_{max} = 7.7$) and 2ndSAV ($\Delta t_{max} = 3.0$) schemes are 13 times and 5 times greater than those of the widely-used referencing SI schemes. In addition, for both SI and SAV simulations, the 2^{nd} order BDF scheme is more accurate than the 1^{st} order BDF scheme at small Δt ($\Delta t < 0.6$ for SI and $\Delta t < 0.2$ for SAV). However, for SAV simulations with larger Δt, the 1^{st} order BDF scheme is more accurate due to the local truncation errors of the numerical schemes. For $\Delta t \ll 1$, the local truncation error for the 2^{nd} order BDF is second order in time, whereas the higher order terms of Δt become dominant when Δt becomes larger. As a result, its accuracy drops faster than the 1^{st} order BDF scheme. In this sense, although the

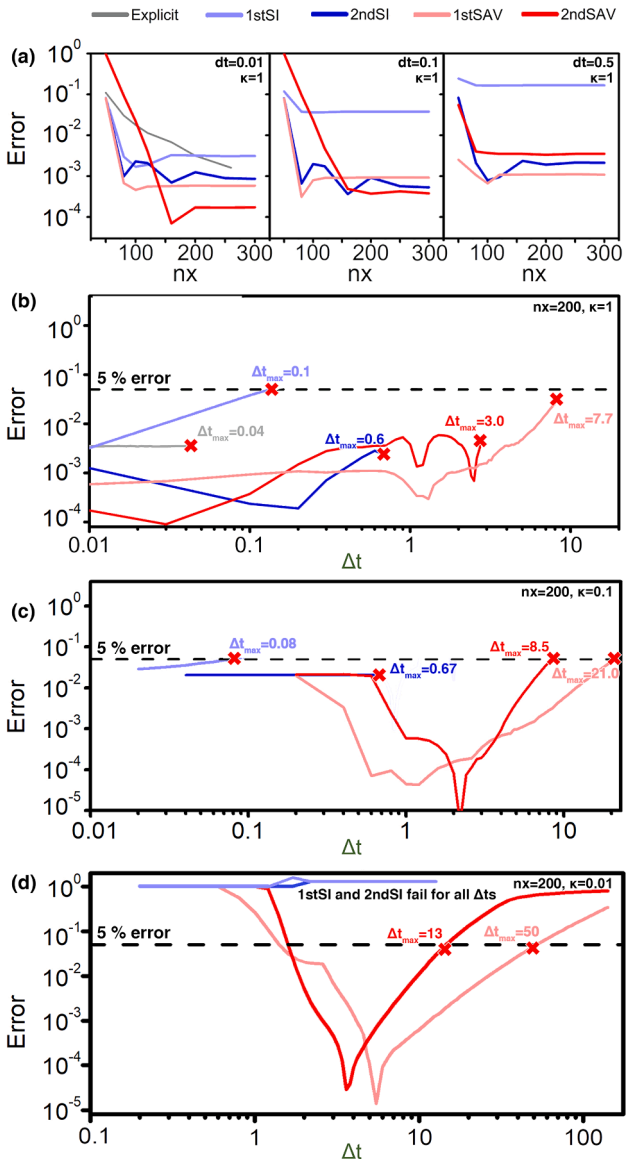

Fig. 2. Simulation results for 3D single spherical grain shrinking problem. (a) the error plots as function of nx (Δx) while Δt is fixed at 0.01, 0.1 and 0.5, respectively. All the errors in the plots are calculated as $|1-\mathscr{R}|$. (b)-(d) The error plot as function of Δt for different discretization schemes within $100\times 100\times 100$ system and $nx=200$ ($\Delta x=0.5$) for $\kappa=1, 0.1$ and 0.01, respectively. The other parameters used can be found in Table 1. Besides, the simulation is considered incorrect and the corresponding plot is marked with red cross thereafter if the error is greater than 5% or the maximum value of the order parameter in the bulk deviates by 5%.

accuracy of the domain-shrinking problem can only be strictly guaranteed under small Δt and fixed Δx, our current benchmark simulations show that under given accuracy requirements, the SAV schemes allows a much larger Δt for stable numerical solutions.

For cases with thinner interfaces, e.g., $\kappa=0.1$ shown in Fig. 2 (c), while the referencing semi-implicit schemes are accurate with a limited Δt, the SAV schemes are accurate with a larger maximum Δt compared with the $\kappa=1$ case. For extremely thin interfaces shown in Fig. 2 (d), i.e., $\kappa=0.01$, the semi-implicit schemes fail to provide accurate results for all Δt values whereas the SAV schemes overcome numerical pinning and provide accurate domain shrinking trend for $\Delta t>1.5$ and remain accurate up to Δt as large as 50. The results show a greater advantage for the SAV schemes over the semi-implicit schemes on the thinner interfaces.

3.2. 3D grain growth with multiple grains

In this section, the SAV scheme is applied to polycrystal growth with multiple order parameters. The performance of the SAV based schemes (1stSAV and 2ndSAV) are compared with the well-established explicit, 1stSI and 2ndSI reference schemes. These reference schemes demonstrate very good efficiency in different works for the last two decades [6,9,18,30,31].

We consider a general 3D inhomogeneous system consisting of multiple grains, where a set of phase-field variables $\eta_1,\eta_2,\cdots,\eta_N$ are used to represent each of these grains. A simplest form of f for such a model system as a function of the phase-field variables is [23,24]:

$$f(\{\eta_i\}) = -\frac{1}{2}\sum_q^N \eta_q^2 + \frac{1}{4}\left(\sum_q^N \eta_q^2\right)^2 + \frac{1}{2}\sum_q^N\sum_{p>q}^N \eta_p^2\eta_q^2. \tag{24}$$

In this case, $f(\{\eta_i\})$ has $2N$ degenerated minima located at $(\pm 1,0,\cdots,0)$, $(0,\pm 1,\cdots,0),\ldots,(0,0,\cdots,\pm 1)$. The evolution of these order parameters is governed by Allen-Cahn equations, i.e., $x=0$ in Eq. (2). The discretization of the governing equations involving multiple phase-field variables based on SAV scheme is similar to that of single phase-field variable as described in Section 3.1, by applying partial derivatives of non-linear free energy expression $\partial f(\{\eta_i\})/\partial\eta_i$ following Eq. (24) into Eq. (8), one would evolve Eqs. (17) and (18) as the governing equations for the grain-growth model within SAV scheme.

The simulations are performed with parameters listed in Table 2. The system is initialized with a total of N spherical grain seeds with a uniform radius r_{seed} located at random positions. That is, for the i-th particle with an initial radius r_{seed} and center position vector ℓ_0, the order parameter η_i is initialized as: $\eta_i,\ (\ell-\ell_0\leqslant r_{seed})|_{t=0}=1, \eta_i(\ell-\ell_0>r_{seed})|_{t=0}=0$. The matrix phase is defined after the system initialization as the mesh points with no finite grain order parameters. To avoid unnecessary numerical issues, no more than one finite grain order parameter is assigned to a certain mesh point. Periodic boundary condition (PBC) is applied along x-, y- and z- directions of the simulation domain. Fig. 3 shows the comparison of 1stSAV and 2ndSI schemes with $\Delta t=0.1$ on the morphology of the grains using $\Delta x=1$ ($nx=100$) and the same initial random seeds. According to Fig. 3 (a)-(h), the SAV based simulation yields an identical evolution process with the reference numerical scheme. Fig. 3 (i) plots the average grain sizes as functions of time for the model with the two different schemes. The figure demonstrates that the model with SAV schemes show consistent results with the model with referencing 2ndSI scheme. Table 3 lists the maximum Δt for each scheme based on the same initial condition and the following accuracy judging criteria: i) the maximum summation of order parameters $\sum_i\eta_i^2$ must lie in [0.95, 1.05], ii) the average grain diameter should not deviate more than 10% compared with an accurate reference. According to Table 3, SAV schemes show better performance than explicit and semi-implicit schemes with a maximum accurate Δt being 1.2 for 1stSAV and 1.7 for 2ndSAV, but the advantage drops to about 2 times. According to Eq. (5), r serves as the prefactor for the gradient term in the evolution equation. For the case where only one order parameter is evolving ($N=1$), the convergence is greatly enhanced since the coefficient $r/\sqrt{\mathscr{F}_L+C_0}$ changes with time to balance the local and gradient driving forces. However, for grain growth involving multiple grain order parameters, one r cannot account for the evolutions of all the order parameters as accurately as the single grain case, so the maximum accurate Δt for SAV scheme cannot be as large as that of the single crystal case.

Table 2
Parameters used in the 3D grain growth simulation.

κ	L	N	$Lx(=Ly=Lz)$	$\Delta x(=\Delta y=\Delta z)$	Δt	r_{seed}
2	1	100	100	0.33–3.3	0.001–6.0	10

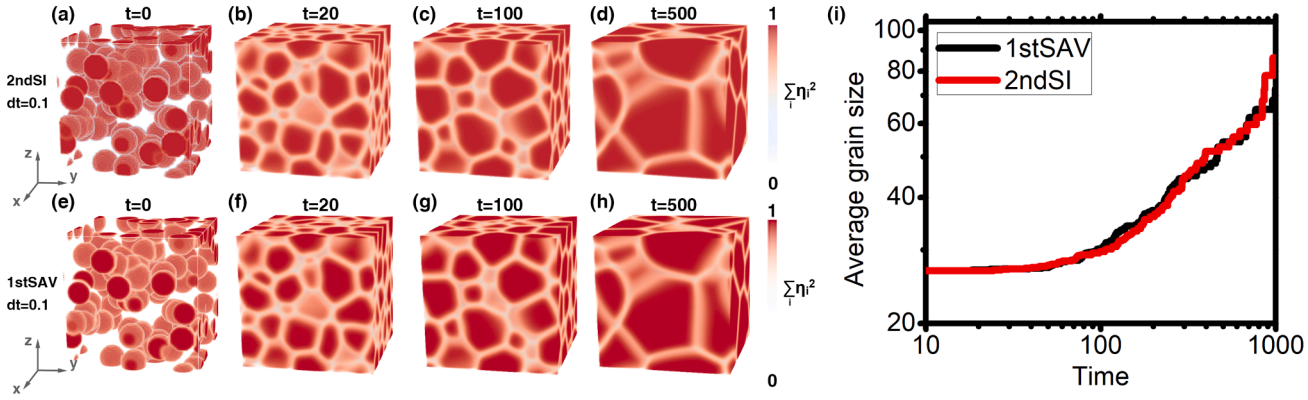

Fig. 3. Simulation results for polycrystalline evolution starting from the same initial condition with identical nuclei for the 1stSAV scheme and 2ndSI scheme. Both simulations use $\Delta t = 0.1$ and $\Delta x = \Delta y = \Delta z = 1$. (a)-(h) the morphological plots for the reference 2ndSI model and the SAV based model at $t = 0$, 20, 100 and 500, respectively. (i) the average grain size as functions of simulation time for the SAV based model and the reference 2ndSI model.

Table 3
Efficiency and accuracy comparison for the SAV based models and the reference models on the multi-grain growth problems. The simulations use identical initial grain seed distribution and the $\Delta x = \Delta y = \Delta z = 1$ for all simulation cases. The maximum Δt is obtained using two judging criterions: i) the maximum summation of order parameters $\sum_i \eta_i^2$ must lie in [0.95, 1.05], ii) the average grain size should not deviate more than 10% when the number of active grains is larger than 10.

Scheme	Explicit	1stSI	2ndSI	1stSAV	2ndSAV
Max Δt	0.08	1.0	0.6	1.2	1.7

3.3. Spinodal decomposition problem

Spinodal decomposition describes the spontaneous separation of an unstable solution to form multiple composition domains, which can be described by the Cahn-Hillard (CH) equation. For a general 3D inhomogeneous system with a single composition field η, we adopt Eq. (19) and Eq. (21) as a simple form of f and its derivative. For this spinodal decomposition problem, we have $\mathscr{G} = \Delta L$ in Eq. (2), so the evolution equation becomes

$$\frac{\partial \eta}{\partial t} = L\Delta(-\kappa\Delta\eta + f'(\eta)). \tag{25}$$

The discretized evolution equations using 1st order BDF based SAV scheme can be expressed as

$$\frac{\eta^{n+1} - \eta^n}{\Delta t} = L\Delta\left(-\kappa\Delta\eta^{n+1} + \frac{r^{n+1}}{\sqrt{f(\eta^{n+1}) + C}} f'(\eta^{n+1})\right), \tag{26}$$

The evolution of r is governed by Eq. (23). The numerical solutions are expressed in Eqs. (17) and (18). For the other schemes (i.e., 2ndSAV, 1stSI and 2ndSI) used in this Section, please refer to supplementary material S4 for the detailed implementations.

The SAV scheme for spinodal decomposition is firstly tested by comparing with an accurate 1D reference with spatiotemporal evolution profiles, using parameters listed in Table 4. This reference profile uses 1stSI scheme with $\Delta x = 0.5$ and $\Delta t = 0.02$. The accuracy of this reference profile is validated by performing a series of testing simulations with smaller Δx, Δt and different numerical schemes; and then finding the maximum relative error $\mathscr{E}$ between the testing profiles and the reference profile at all positions and simulation times. As shown in Table 5, the reference case shows no more than 3×10^{-3} difference compared to either the cases with smaller Δt and/or Δx with the same numerical scheme or the cases with the same Δt and Δx but different numerical schemes. These results validate the accuracy of the reference case and indicate the four numerical schemes in Table 5 are consistent at small Δx and Δt. The validated reference is then compared with simulation cases with different Δt and numerical schemes. The results are shown in Fig. 4. The allowable error threshold is set to 5%, as shown by the dashed grey line in Fig. 4. According to the results, the SAV schemes are shown to be accurate and consistent for a range of Δt values up to 0.60, similar to SI schemes.

3D simulations of spinodal decomposition are then performed using different numerical schemes with different Δt and the parameters in Table 4. The initial composition corresponds to uniform distribution near 0 with a magnitude of 0.002, i.e., $\eta_{t=0}(\mathscr{l}) \sim U[-0.001, 0.001]$ where $\mathscr{l}$ is the position vector of any mesh points. Due to the sensitivity of the evolved profiles to Δt values, only the criterion $|\eta_{\max} - 1| < 5\%$ is adopted to judge if a simulation is acceptable. The simulation results are summarized in Table 6. According to the results, 2ndSAV scheme simulates with the largest $\Delta t_{\max}$, which is about 1.5–2 times the 1stSI and 1stSAV schemes for $\kappa = 0.1$ and 1 cases while 2ndSI scheme has the smallest $\Delta t_{\max}$. For the case with $\kappa = 0.01$, all numerical schemes with fixed Δt end up with a small $\Delta t_{\max} \approx 0.01$ because of the numerical pinning and large driving force near the thin interfaces. However, with the implementation of the adaptive Δt algorithm [32] (see supplementary material S6 for details), the SAV scheme-based models can be greatly accelerated. The simulation results with 1stSAV + adaptive Δt scheme for $\kappa = 0.01$ are shown in Fig. 5. The results show typical spinodal decomposition patterns. On the other hand, we are not able to increase $\Delta t_{\max}$ using adaptive Δt for the semi-implicit schemes. This can be attributed to the different mechanisms that lead to the failure of the

Table 4
Parameters used in the 1D and 3D spinodal decomposition simulations.

κ	L	N	Δt	Initial profile (1D)
1 (1D), 0.01–1 (3D)	1	1	0.005–5.0	$\eta_0 = \sin\frac{2\pi x}{Lx}, x \in [0, L_x]$
$Lx(=Ly=Lz)$			$\Delta x(=\Delta y=\Delta z)$	
100			0.5	

Table 5
The errors between selected simulation cases and the referencing case for 1D spinodal decomposition problem.

Case No.	Scheme	Δt	Δx	Error $\mathscr{E}$
Ref	1stSI	0.02	0.5	0
1	1stSI	0.005	0.5	1.29×10^{-3}
2	1stSI	0.005	0.25	1.29×10^{-3}
3	2ndSI	0.02	0.5	1.38×10^{-3}
4	1stSAV	0.02	0.5	2.32×10^{-3}
5	2ndSAV	0.02	0.5	1.38×10^{-3}

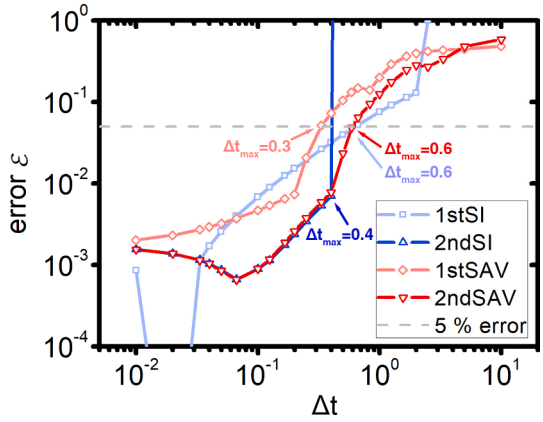

Fig. 4. Comparison between the reference case within 1stSI at $\Delta x = 0.5$, $\Delta t = 0.02$ and the testing cases with 1stSI, 2ndSI, 1stSAV and 2ndSAV numerical schemes at different Δt.

Table 6
The performance of different numerical schemes on 3D spinodal decomposition problems with $\kappa = 0.01, 0.1$ and 1. The $\Delta t_{\max}$ is judged by the criterion $|\eta_{\max} - 1| \langle 5\%$. That is, $\Delta t_{\max}$ is the maximum Δt for certain scheme and κ to satisfy the criterion $|\eta_{\max} - 1| \langle 5\%$ throughout the simulation.

Numerical scheme	Adaptive Δt + SAV	1stSAV	2ndSAV	1stSI	2ndSI
$\Delta t_{\max}$ κ = 0.01	>5	~0.01	~0.01	~0.01	~0.01
$\Delta t_{\max}$ κ = 0.1	>5	0.16	0.31	0.16	0.01
$\Delta t_{\max}$ κ = 1	>5	2.4	3.8	2.0	0.41

SAV and SI schemes under fixed large Δt. For SAV schemes, the limit for the time step size is the large driving force in the early stage of the simulation whereas for SI schemes, the limit for the time step size is the kinetic equations and conditional numerical stability. Since the currently adopted adaptive Δt scheme automatically updates Δt based on the driving force of the previous time step, it works well for SAV schemes using small Δt values at the beginning of the simulation and then increasing to larger values as the driving force decreases for later stages. In contrast, the adaptive Δt + SI schemes could not enjoy such advantage since Δt could not exceed a certain threshold. As a result, with the implementation of adaptive Δt algorithm, the SAV schemes can achieve more than 100-time larger Δt than the semi-implicit Fourier spectral schemes with good accuracy.

3.4. 3D coherent precipitate growth morphology

Precipitation of second-phase particles is a common process in strengthening metallic alloys [33-35]. As an example, we apply the SAV scheme to solve the phase-field equations describing the growth morphology of β'-Mg_7Nd precipitates in Mg-Nd alloys [35]. We employ three structural order parameters to distinguish the three orientation variants of β' precipitates and one composition field (composition of Nd) to describe the compositional distributions in the precipitate-matrix two phase system. The elastic strain energy contribution to the thermodynamic driving force for β' evolution and the anisotropic Mg/β' interfacial energies are considered.

The free energy density, f_{total}, is given by

$$f(x, \{\eta_i\}) = f_{local}(x, \{\eta_p\}) + f_{grad}(\{\nabla\eta_p\}) + f_{el}(\{\eta_p\}), \tag{27}$$

where the order parameter set $\{\eta_p\} = \{\eta_1, \eta_2, \eta_3\}$ represents the spatial distributions of the three structural variants of β' precipitates, $\{\nabla\eta_p\} = \{\nabla\eta_1, \nabla\eta_2, \nabla\eta_3\}$ is the gradient in structural order parameters, and x is the local composition of Nd. In Eq. (27), the free energy density includes the contributions from the gradient energy density $f_{grad}(\{\nabla\eta_p\})$, local bulk energy density $f_{local}(x, \{\eta_p\})$, and elastic energy density $f_{el}(\{\eta_p\})$,

$$f_{local}(x, \{\eta_p\}) = f^{\alpha}(x^{\alpha})\left(1 - \sum_{i=1}^{3} h(\eta_i)\right) + f^{\beta'}(x^{\beta'})\sum_{i=1}^{3} h(\eta_i) + \omega f_{dw}(\{\eta_p\}), \tag{28}$$

$$f_{grad}(\{\nabla\eta_p\}) = \frac{1}{2}\sum_{p=1}^{3}\kappa^{o}_{p,ij}\nabla_i\eta_p\nabla_j\eta_p, \tag{29}$$

$$f_{el} = \frac{1}{2}C_{ijkl}\left(\bar{\varepsilon}_{ij} + \delta\varepsilon_{ij} - \varepsilon^{0}_{ij}\right)\left(\bar{\varepsilon}_{kl} + \delta\varepsilon_{kl} - \varepsilon^{0}_{kl}\right). \tag{30}$$

In Eq. (28), f^{α}, $f^{\beta'}$, x^{α} and $x^{\beta'}$ are the free energy densities and Nd compositions in α-Mg (matrix) phase and β' precipitate phase, respectively, $h(\eta_i) = 3\eta_i^2 - 2\eta_i^3$ is the interpolation function, and f_{dw} is a double-well type potential, with ω being the barrier height. The Kim-Kim-

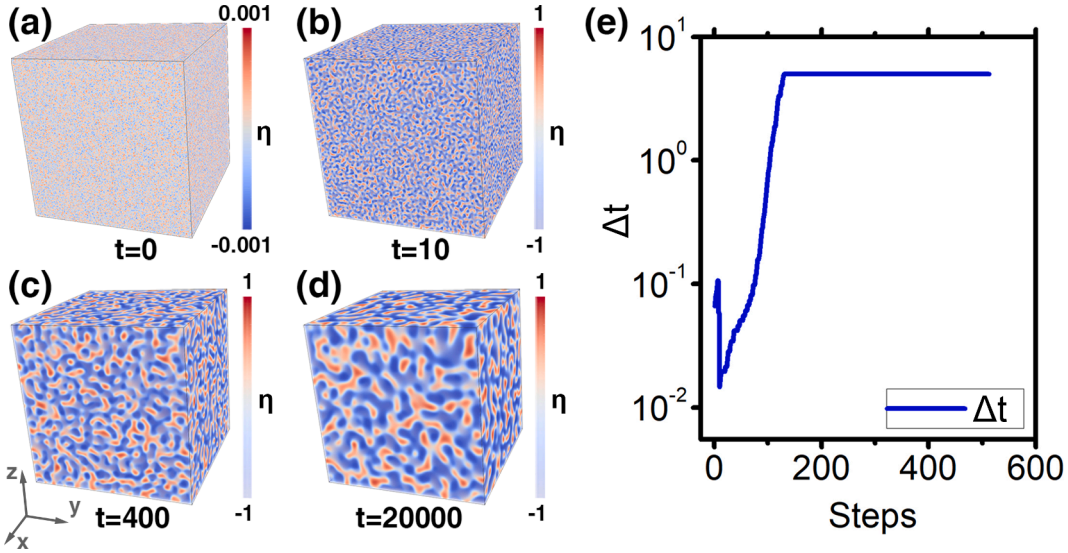

Fig. 5. 3D spinodal simulation results based on 1stSAV + adaptive Δt scheme for $\kappa = 0.01$. (a)-(d) evolutionary profiles for the order parameter at $t = 0$, 10, 400 and 20,000, respectively. (e) the Δt-steps profile, indicating an increasing Δt trending for simulations based on SAV schemes, the Δt is manually bounded from above at $\Delta t = 5$.

Suzuki model [36] is adopted to compute the compositions in each phase. Eq. (29) describes the gradient energy density, and $\kappa^{o}_{p,ij}$ are the anisotropic gradient coefficients. Eq. (30) is the elastic energy density which can be obtained based on the microelasticity theory of Khachaturyan *et al.* [37].

Based on Eq. (27), the evolution equations for composition and order parameters are:

$$\frac{\partial x}{\partial t} = \nabla \cdot M \nabla \left(\frac{\partial f_{local}(\{\eta_p\}, x)}{\partial x} \right), \tag{31}$$

$$\frac{\partial \eta_p}{\partial t} = -L\left(\frac{\partial f_{local}}{\partial \eta_p}(\{\eta_p\}, x) - \sum\nolimits_{i,j}^{3} \kappa^{o}_{p,ij} \nabla_i \nabla_j \eta_p + \frac{\partial f_{el}}{\partial \eta_p}(\{\eta_p\}) \right), \tag{32}$$

To implement the SAV scheme, we solve the Allen-Cahn equation (Eq. (32)) with $\mathscr{G} = -L$ and the Cahn-Hillard diffusion equation with $\mathscr{G} = \Delta M$ (Eq. (31)) with gradient coefficient $\kappa = 0$. For evolving the scalar r, we use $f = f_{local}(x, \{\eta_p\}) + f_{el}(\{\eta_p\})$ in calculating Eq. (4) and (11).

With the SAV scheme, we perform a 3D phase-field simulations of β' growth morphology. Three orientations of precipitates with 24 nuclei each are initially introduced in a 200 Δx*200 Δx*200 Δx (grid size: $\Delta x = 0.25$ nm) system with randomized distribution and size. The initial Nd composition is $x_0 = 0.00625$. Other simulation parameters can be found in reference [35].

Fig. 6 (a) – (c) are the evolution profiles of the β' precipitates. It is shown that the growth of the precipitate is anisotropic arising from the elastic interactions and the anisotropic interfacial energy. To quantify the accuracy and efficiency of the SAV scheme in solving the coupled Allen-Cahn equation, diffusion equation, and the mechanical equilibrium equation, we employed the following two judging criteria: The model is considered accurate only when (1) the maximum value of any order parameter $\eta_{i,\max}$ deviates no more than 5% from the equilibrium value 1, and (2) the volume fraction $V_f(t)$ should not deviate more than 10% from the reference case where semi-implicit Fourier spectral scheme with $dt = 10^{-4}$ is used. Fig. 6 (d) shows the efficiency comparison of SAV-based and semi-implicit Fourier spectral scheme-based (*abbr.* SI-based) simulations. Both simulations are performed using 1 core in AMD EPYC Processor located at Bridges-2 server, and the details of efficiency comparison between the two schemes are summarized in Table 7. According to the simulations, the maximum order parameter $\eta_{i,\max}$ decreases in SI-based simulations after the initial relaxation of the model, which violates judging criterion (1) at and beyond $dt \approx 0.001$ whereas the SAV-based simulations show good convergence in $\eta_{i,\max}$ until $dt \approx 0.07$ (See supplemental material S7 for more information). Meanwhile, both simulations follow criterion (2) even for the aforementioned extreme cases for criterion (1), as shown in the inset of Fig. 6 (d). On the other hand, the average CPU time cost per step in SAV-based simulations is 92% compared with that of SI-based simulations, indicating a 76-time overall efficiency enhancement of the SAV scheme over the SI scheme.

Table 7
The performance comparison between the SAV scheme- and semi-implicit Fourier spectral scheme (SI)-based simulations of β'-Mg_7Nd precipitate evolution in Mg-Nd alloys. Δt_{max} represents the maximum time step that satisfies both following criteria (1) and (2) $|\eta_{max} - 1| < 5\%$ volume fraction V_f of precipitates should not deviate 10% at any time compared with a reference simulation with small Δt. The factors restricting the application of larger Δt are also summarized herein.

Numerical scheme	Δt_{max}	Δt_{max} restricted by	Time used per step (SI = 1)	Efficiency (SI = 1)
SAV	0.07	Criterion (1):$\lvert\eta_{max} - 1\rvert < 5\%$	0.92	76
SI	0.001	Criterion (1):$\lvert\eta_{max} - 1\rvert < 5\%$	1	1

4. Discussions

We demonstrated dramatic efficiency enhancement by implementing the SAV scheme with the semi-implicit spectral scheme which is one of the most efficient schemes for solving phase-field equations. However, to ensure the performance enhancement of the SAV scheme, it is important to consider the following two important strategies.

1. Adaptive time stepping: Although the SAV based schemes show unconditional energy stability regardless of Δt, large Δt values could lead to inaccurate simulation results such as abnormal morphology and incorrect kinetics. As discussed in Section 3.3, the implementation of an adaptive Δt algorithm could potentially mitigate or even eliminate such issues, but the Δt value used in the simulation still needs to be carefully selected. In addition to the example in Fig. 5, another example is the inaccurate grain growth behavior predicted by the SAV model with $\Delta t > 5$ in the incipient stage of polycrystal growth ($t < 100$). In this case, the bulk driving force is large when the matrix is present while the driving force significantly decreases after the matrix is fully consumed by the grains ($t > 100$). To overcome this issue, the adaptive Δt algorithm may be implemented with care to ensure the accuracy of the model at start using smaller Δt, while increasing Δt when the driving force decreases to accelerate the simulation with adequate accuracy. Details of adaptive Δt algorithm has been reported in ref. [29], and it is shown to work well when the criteria for adapting Δt are correctly chosen. In addition, while using adaptive Δt, one should keep in mind that Eq. (10) should be modified for the explicit approximation of order parameters for the

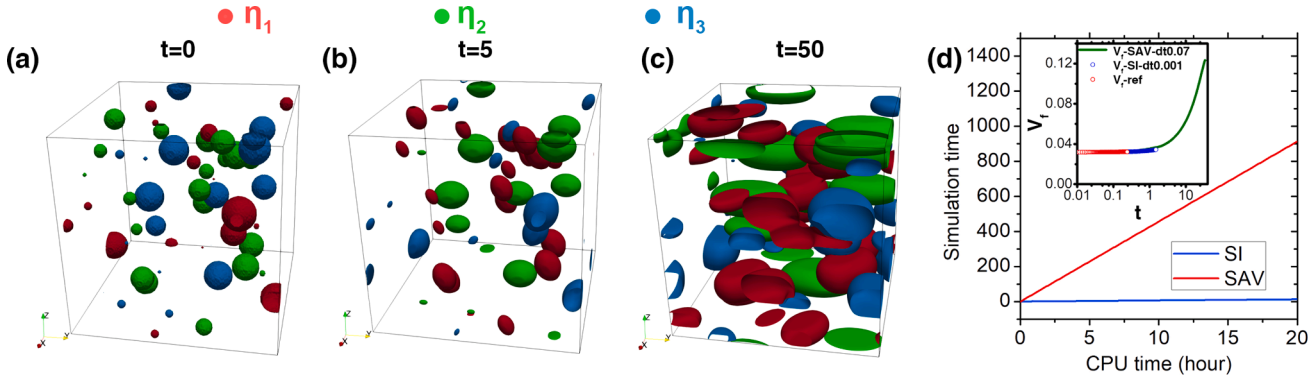

Fig. 6. 3D evolutionary profiles for β' precipitations in Mg-Nd alloy. (a)-(c) evolutionary profiles for the order parameters at $t = 0$, 5 and 50, respectively. (d) Efficiency comparison between SI-based and SAV-based simulations based on the same accuracy judging criteria. The inset shows the evolution of volume fraction of the precipitates by different simulations compared with the referencing simulation.

next time step, that is, Δt is different for n-1$^{\text{th}}$ step and n^{th} step, so that the Δt values should be applied to weigh Eq. (10) if a constant temporal derivative for η is assumed for the next-step approximation of η. Also, the accuracy of the simulation may be very sensitive to the selection of the Δt across steps.

2. Proper splitting of the free energy: For the simulation cases where the absolute value of the non-gradient term $F(\{\eta_i\})$ is much higher than that of the gradient term, e.g., grain growth with a small gradient energy coefficient κ, the simulation can become unreliable with large Δt values. In this situation, one may split the free energy expression of the grain growth model [29] as follows:

$$\mathscr{F} = \int_V \left[\left(F(\{\eta_i\}) - \sum_N^q S\eta_q^2 \right) + \sum_q^N \left(\frac{\kappa_q}{2}\nabla^2\eta_q + S\eta_q^2 \right) \right] \mathrm{d}V \tag{33}$$

where a positive parameter S is introduced in order to reduce the impact of the non-gradient term. The evolution equations remain similar to Eqs. (17) and (18) despite differences in the expression of r based on Eq. (4) and the definition of matrix $\mathbf{M}$ in Eq. (14). This modification can be very effective for problems with thin interfaces [29].

In addition, a multiple scalar auxiliary variable (MSAV) scheme is recently proposed by Cheng et al. [38] which offers another strategy to improve the performance of the SAV scheme when the nonlinear terms consist of multiple disparate terms. This scheme enjoys the same accuracy and efficiency as the SAV scheme with multiple new scalar auxiliary variables to represent the multiple disparate nonlinear terms. Recently, the SAV scheme has been extended by introducing a Lagrange multiplier [39] and then generalized to a function including a given invertible function [40] instead of an auxiliary variable. This helps evolve the governing order parameter without the restriction that the non-linear energy should be bounded below. Thus, the SAV scheme is generally applicable to enhance the performance of a wide range of phase-field simulations.

5. Conclusions

We implemented the scalar auxiliary variable (SAV) scheme for solving the phase-field equations. It is demonstrated that the SAV scheme can be more than an order of magnitude more efficient than the state-of-the-art semi-implicit Fourier-spectral scheme for a single Allen-Cahn equation and a 100% improvement for multiple Allen-Cahn equations. It is demonstrated that this improvement becomes more dramatic as the interfaces become thinner. Combining with an adaptive time-stepping, the implemented SAV scheme is shown to be about two orders of magnitude more efficient over semi-implicit Fourier spectrum scheme for solving the Cahn-Hilliard equation. In addition, the SAV scheme is adopted to predict the diffusion-controlled evolution of alloy precipitates with strain energy contributions, which demonstrates more than 50-time acceleration over the semi-implicit Fourier spectral scheme. The implementation and test results in this work highlight the potential of the SAV scheme in enhancing the efficiency for simulating a broad range of phase-field models due to its stability and versality.

Declaration of Competing Interest

The authors declare that they have no known competing financial interests or personal relationships that could have appeared to influence the work reported in this paper.

Data Availability

Most data required to reproduce the results and findings are included in tables or texts in this paper, while some data included in other works are cited and explicitly stated in text. Part of raw data required to reproduce these findings cannot be shared at this time as the data also forms part of an ongoing study.

Acknowledgement

The work at Penn State is supported by the US National Science Foundation under the grant number DMR-1744213. L.-Q. Chen also acknowledges the support from the Hamer Professorship at Penn State. The effort at Purdue University is partially supported by NSF Grant DMS-2012585 and AFOSR Grant FA9550-20-1-0309. The simulations were supported by the Extreme Science and Engineering Discovery Environment (XSEDE) which is supported by the National Science Foundation under grant ACI-1548562.

Appendix A. Supplementary material

Supplementary data to this article can be found online at https://doi.org/10.1016/j.commatsci.2022.111556.

References

[1] L.-Q. Chen, Phase-field models for microstructure evolution, Annu. Rev. Mater. Res. 32 (1) (2002) 113–140.
[2] G. Demange, H. Zapolsky, R. Patte, M. Brunel, A phase field model for snow crystal growth in three dimensions, npj Comput. Mater. 3 (1) (2017) 15.
[3] E. Miyoshi, T. Takaki, M. Ohno, Y. Shibuta, S. Sakane, T. Shimokawabe, T. Aoki, Ultra-large-scale phase-field simulation study of ideal grain growth, npj Comput. Mater. 3 (1) (2017) 25.
[4] V. Badalassi, H. Ceniceros, S. Banerjee, Computation of multiphase systems with phase field models, J. Comput. Phys. 190 (2) (2003) 371–397.
[5] C. Chen, X. Yang, Efficient numerical scheme for a dendritic solidification phase field model with melt convection, J. Comput. Phys. 388 (2019) 41–62.
[6] L.Q. Chen, J. Shen, Applications of semi-implicit Fourier-spectral method to phase field equations, Comput. Phys. Commun. 108 (2–3) (1998) 147–158.
[7] M. Cheng, J.A. Warren, An efficient algorithm for solving the phase field crystal model, J. Comput. Phys. 227 (12) (2008) 6241–6248.
[8] C.M. Elliott, A. Stuart, The global dynamics of discrete semilinear parabolic equations, SIAM J. Numer. Anal. 30 (6) (1993) 1622–1663.
[9] J. Gruber, N. Ma, Y. Wang, A.D. Rollett, G.S. Rohrer, Sparse data structure and algorithm for the phase field method, Modell. Simul. Mater. Sci. Eng. 14 (7) (2006) 1189.
[10] F. Guillén-González, G. Tierra, On linear schemes for a Cahn-Hilliard diffuse interface model, J. Comput. Phys. 234 (2013) 140–171.
[11] Y. He, Y. Liu, T. Tang, On large time-stepping methods for the Cahn-Hilliard equation, Appl. Numer. Math. 57 (5–7) (2007) 616–628.
[12] J. Shen, Efficient spectral-Galerkin method I. Direct solvers of second-and fourth-order equations using Legendre polynomials, SIAM J. Sci. Comput. 15 (6) (1994) 1489–1505.
[13] J. Shen, Efficient spectral-Galerkin method II. Direct solvers of second-and fourth-order equations using Chebyshev polynomials, SIAM J. Sci. Comput. 16 (1) (1995) 74–87.
[14] J. Shen, J. Xu, J. Yang, The scalar auxiliary variable (SAV) approach for gradient flows, J. Comput. Phys. 353 (2018) 407–416.
[15] J. Shen, X. Yang, An efficient moving mesh spectral method for the phase-field model of two-phase flows, J. Comput. Phys. 228 (8) (2009) 2978–2992.
[16] J. Shen, X. Yang, A phase-field model and its numerical approximation for two-phase incompressible flows with different densities and viscosities, SIAM J. Sci. Comput. 32 (3) (2010) 1159–1179.
[17] J. Shen, X. Yang, Numerical approximations of Allen-Cahn and Cahn-Hilliard equations, Discrete Contin. Dynam. Syst.-A 28 (4) (2010) 1669.
[18] L. Vanherpe, N. Moelans, B. Blanpain, S. Vandewalle, Bounding box algorithm for three-dimensional phase-field simulations of microstructural evolution in polycrystalline materials, Phys. Rev. E 76 (5) (2007) 056702.
[19] S. Vedantam, B. Patnaik, Efficient numerical algorithm for multiphase field simulations, Phys. Rev. E 73 (1) (2006) 016703.
[20] B.P. Vollmayr-Lee, A.D. Rutenberg, Fast and accurate coarsening simulation with an unconditionally stable time step, Phys. Rev. E 68 (6) (2003) 066703.
[21] X. Yang, Linear, first and second-order, unconditionally energy stable numerical schemes for the phase field model of homopolymer blends, J. Comput. Phys. 327 (2016) 294–316.
[22] S.-L. Wang, R.F. Sekerka, Algorithms for phase field computation of the dendritic operating state at large supercoolings, J. Comput. Phys. 127 (1) (1996) 110–117.
[23] D. Fan, L.-Q. Chen, Computer simulation of grain growth using a continuum field model, Acta Mater. 45 (2) (1997) 611–622.
[24] C. Krill Iii, L.-Q. Chen, Computer simulation of 3-D grain growth using a phase-field model, Acta Mater. 50 (12) (2002) 3059–3075.
[25] Y. Li, S. Hu, Z. Liu, L. Chen, Effect of substrate constraint on the stability and evolution of ferroelectric domain structures in thin films, Acta Mater. 50 (2) (2002) 395–411.
[26] T. Tang, H. Yu, T. Zhou, On energy dissipation theory and numerical stability for time-fractional phase-field equations, SIAM J. Sci. Comput. 41 (6) (2019) A3757–A3778.

[27] A. Bouchriti, M. Pierre, N.E. Alaa, Remarks on the asymptotic behavior of scalar auxiliary variable (sav) schemes for gradient-like flows, J. Appl. Anal. Comput. 10 (5) (2020) 2198–2219.
[28] X. Cheng, D. Li, K. Promislow, B. Wetton, Asymptotic behaviour of time stepping methods for phase field models, J. Sci. Comput. 86 (3) (2021) 1–34.
[29] J. Shen, J. Xu, J. Yang, A new class of efficient and robust energy stable schemes for gradient flows, SIAM Rev. 61 (3) (2019) 474–506.
[30] K. Chang, W. Feng, L.-Q. Chen, Effect of second-phase particle morphology on grain growth kinetics, Acta Mater. 57 (17) (2009) 5229–5236.
[31] S.G. Kim, Y.B. Park, Grain boundary segregation, solute drag and abnormal grain growth, Acta Mater. 56 (15) (2008) 3739–3753.
[32] H. Gomez, T.J. Hughes, Provably unconditionally stable, second-order time-accurate, mixed variational methods for phase-field models, J. Comput. Phys. 230 (13) (2011) 5310–5327.
[33] T. Baiatu, R. Waser, K.H. Härdtl, Dc electrical degradation of perovskite-type titanates: III, a model of the mechanism, J. Am. Ceram. Soc. 73 (6) (1990) 1663–1673.
[34] J.E. Guyer, W.J. Boettinger, J.A. Warren, G.B. McFadden, Phase field modeling of electrochemistry, I. Equil., Phys. Rev. E 69 (2) (2004) 021603.
[35] Y. Ji, A. Issa, T. Heo, J. Saal, C. Wolverton, L.-Q. Chen, Predicting β′ precipitate morphology and evolution in Mg–RE alloys using a combination of first-principles calculations and phase-field modeling, Acta Mater. 76 (2014) 259–271.
[36] S.G. Kim, W.T. Kim, T. Suzuki, Phase-field model for binary alloys, Phys. Rev. E 60 (6) (1999) 7186.
[37] A.G. Khachaturyan, Theory of structural transformations in solids, Courier Corp. (2013).
[38] Q. Cheng, J. Shen, Multiple scalar auxiliary variable (MSAV) approach and its application to the phase-field vesicle membrane model, SIAM J. Sci. Comput. 40 (6) (2018) A3982–A4006.
[39] Q. Cheng, C. Liu, J. Shen, A new Lagrange multiplier approach for gradient flows, Comput. Methods Appl. Mech. Eng. 367 (2020) 113070.
[40] Q. Cheng, C. Liu, J. Shen, Generalized SAV approaches for gradient systems, J. Comput. Appl. Math. 394 (2021) 113532.